https://doi.org/10.5194/egusphere-2026-5139
Preprint. Discussion started: 9 September 2026

RADALIA: A new tool for dealiasing Doppler cloud radar observations

Matheus Tolentino[1,2], Lukas Pfitzenmaier[3], Tuomas Siipola[4], Ewan O'Connor[4], Simo Tukiainen[4], Juan Antonio Bravo-Aranda[1,2], Lucas Alados-Arboledas[1,2], and Maria José Granados-Muñoz[1,2]

[1]Department of Applied Physics, University of Granada, Granada, 18072, Spain
[2]Andalusian Institute for Earth System Research, Granada (IISTA-CEAMA), 18006, Spain
[3]Institute of Geophysics and Meteorology, University of Cologne, Cologne, Germany
[4]Finnish Meteorological Institute, Helsinki, FI-00101, Finland

Correspondence: Maria José Granados-Muñoz (mjgranados@ugr.es)

Abstract. Doppler cloud radars provide valuable insights into cloud dynamics and microphysical processes. However, their measurements are often affected by velocity aliasing when hydrometeor motions exceed the radar Nyquist velocity. Aliasing affects Doppler velocity spectra (DVS) and the derived spectral moments, introducing uncertainties in cloud classification and microphysical retrievals. Despite its importance, a dedicated dealiasing algorithm for cloud radar observations is not yet available. We present RADALIA (RAdar De-ALIsing Algorithm), a new open-source tool designed to detect and correct aliasing in Doppler cloud radar spectra. RADALIA includes two complementary approaches: an interpolation-based method (IntB) that can operate with either single-frequency (i.e., standalone) or dual-frequency observations, and an iterative method based on vertical continuity (IterBU) that operated on single-frequency observations. The algorithms were assessed using dual-frequency cloud radar observations at two ACTRIS CCRES stations: AGORA in Granada (Spain) and JOYCE in Jülich (Germany), representing contrasting atmospheric conditions and levels of dealiasing complexity. The dual-frequency configuration was used as a reference, since it provides the most robust performance in complex situations involving strong attenuation and multiple hydrometeor populations. Under straightforward spectral conditions, all standalone approaches successfully dealiased the DVS, achieving 98.6 %–99.6 % agreement with the dual-frequency reference. In the most challenging spectral scenario, standalone approaches achieved success rates above 70 %. RADALIA addresses a longstanding gap in cloud radar processing and serves as the basis for the dealiasing algorithm being implemented within the Cloudnet processing chain. It has the potential to improve cloud radar products and their application to microphysical retrievals, model evaluation, and satellite validation. Future work will focus on broader validation and extension to additional cloud radar systems and scanning observations.

1 Introduction

Doppler cloud radars are state-of-the-art instruments for studying cloud structure and processes (Küchler et al., 2017; Luke and Kollias, 2013; Kollias et al., 2020). By providing high-resolution Doppler moments and polarimetric variables, these radars offer unique insights into cloud dynamics and microphysics, such as ice crystal growth (Unal and Moisseev, 2004; Kneifel et al., 2016; Oue et al., 2018; Luke et al., 2021; von Terzi et al., 2022; Pfitzenmaier et al., 2018). Additionally, ground-based

https://doi.org/10.5194/egusphere-2026-5139
Preprint. Discussion started: 9 September 2026

radar networks, such as Cloudnet (Illingworth et al., 2007; Tukiainen et al., 2020), within the Aerosols, Clouds and Trace gases Research Infrastructure (ACTRIS, Laj et al., 2024), can provide microphysical retrievals and atmospheric target classification products through instrument synergy, supporting the evaluation of forecast models and an increasing number of satellite products (Pfitzenmaier et al., 2025; Feuillard et al., 2026). However, Doppler radars are affected by the Doppler dilemma: to achieve a broader sampling range, the maximum unambiguous velocity (Nyquist velocity) is reduced. This causes velocity aliasing when the velocity of a moving target is faster than the hardware-defined Nyquist velocity, introducing ambiguity into the Doppler spectrum moments: mean Doppler velocity V_{M}, spectral width S_{w}, skewness S_{skew}, and kurtosis S_{kurt}. This, for example, complicates hydrometeor classification since it affects the shape of the Doppler spectrum and causes particles to appear at incorrect velocities (Unal and Moisseev, 2004; Maahn and Kollias, 2012). The aliased velocity spectrum can affect microphysical retrievals such as the characteristic drop diameter retrieval proposed by Benjamin M. Courtier et al. (2024). In this context, accurate dealiasing of Doppler velocities is critical to extract coherent information from cloud radars, providing high-quality data even when the Nyquist velocity is exceeded (Maahn and Kollias, 2012).

Algorithms for dealiasing weather radar data have been widely developed (e.g., Ray and Ziegler, 1977; Bergen and Albers, 1988; Joe and May, 2003; Haase and Landelius, 2004). Ray and Ziegler (1977) assumed that velocities at all range bins follow a Gaussian distribution, limiting its applicability to simple aliasing cases (Unal and Moisseev, 2004). Bargen and Brown (1980) improved this assumption by enforcing continuity between range gates and assuming that the first range gate is unaliased. However, this method can fail under strong wind conditions, which may violate the unaliased-first-gate assumption. Bergen and Albers (1988) applied vertical continuity and emphasized the importance of removing low signal-to-noise ratio (SNR) bins to avoid false gradients that could be erroneously attributed to aliasing. Further studies have attempted to incorporate auxiliary wind information to improve the first guess. For example, Hennington (1981) and Eilts and Smith (1990) incorporated wind profiles derived from atmospheric soundings. Merritt (1984) relied on a wind model, and Jing and Wiener (1993) used velocity-azimuth display (VAD) wind profiles. Nevertheless, these approaches can fail to represent the complexity of real atmospheric wind fields. James and Houze (2001) incorporated time continuity by using previously dealiased gates as references for correcting subsequent ones. They developed a four-dimensional dealiasing method that incorporates continuity in time, elevation, azimuth, and range. By constraining dealiasing across multiple dimensions, the algorithm reduces dependence on auxiliary wind information (Bergen and Albers, 1988; James and Houze, 2001). However, incorporating continuity across multiple dimensions can significantly increase computational cost, preventing the algorithm from operating in real time or in large datasets. Despite advances in weather radar dealiasing, dedicated cloud radar dealiasing has not yet been addressed, even though they are affected by more severe velocity folding because of their lower Nyquist velocities. This is likely because cloud radar Doppler velocity spectra (DVS) are more complex and may exhibit multiple spectral peaks (Vogl et al., 2024), violating assumptions used in weather radar dealiasing to estimate the reference mean Doppler velocity (i.e., the first guess).

This study presents RADALIA (the RAdar De-ALIsing Algorithm), a promising new open source tool for Doppler cloud radar dealiasing that serves as the basis of Cloudnet dealiasing processing chain, thereby contributing to a high-quality dataset. RADALIA includes two complementary dealiasing methods: an interpolation-based method (IntB) and an iterative bottom-up method (IterBU). The IntB estimates a first-guess velocity either from single-frequency observations through interpolation

https://doi.org/10.5194/egusphere-2026-5139
Preprint. Discussion started: 9 September 2026

and continuity constraints in time (IntB-SF and IntB-SFT, respectively, based on James and Houze, 2001) or from collocated dual-frequency measurements (IntB-DF), where the Ka-band mean Doppler velocity is used as a first-guess for the W-band. In contrast, the IterBU method is a fully standalone single-frequency approach that exploits vertical continuity to iteratively reconstruct folded spectra (based on Bergen and Albers, 1988). Although the described approaches are applied to 94 GHz data in this study, they can also be applied to any other radar frequency separately. Their performance is assessed using two different scenarios: a straightforward one, measured at the JOYCE station under favorable conditions for the dealiasing, and a more complex one, measured at the AGORA station.

This paper is organized as follows. Section 2 presents the Cloudnet stations, datasets, and the dual-frequency cloud radar system. Section 3 provides an overview of FMCW Doppler cloud radar measurements, and the instrumental and physical drivers contributing to the onset of the aliasing issue. Section 4 introduces RADALIA and describes the methodology behind IntB and IterBU methods. Section 5 assesses the performance of the proposed approaches using detailed case studies and one-hour continuous observations from different cloud regimes. Finally, Section 6 summarizes the main conclusions, discusses the strengths and limitations of the algorithm, and provides an outlook on future developments and applications.

2 Cloudnet stations and databases

The JOYCE (Jülich Observatory for Cloud Evolution; Löhnert et al., 2015) and AGORA (Global Atmospheric Observatory of Andalusia; Tolentino et al., 2025; Ortiz-Amezcua et al., 2022) stations were selected because both are equipped with identical dual-frequency Doppler cloud radar (DF-DCR) systems. JOYCE is located in Jülich, Germany (50.91°N, 6.41°E, 110 m asl), in a relatively flat environment with limited topographic influence on cloud dynamics. In contrast, AGORA is located in Granada, Spain (37.16°N, 3.61°W, 680 m asl), within a mountain-valley environment influenced by the Sierra Nevada mountain range and associated local circulations (Ortiz-Amezcua et al., 2022). These contrasting environments provide a suitable framework for assessing RADALIA under different atmospheric conditions and levels of dealiasing complexity.

The DF-DCRs at AGORA and JOYCE (named NEBULA and JOYDURADO, respectively) performed collocated W and Ka band measurements using identical chirp table settings (Table 1). This configuration provides a unique framework for assessing RADALIA under different cloud regimes while minimizing differences arising from instrumental characteristics. In particular, NEBULA and JOYDURADO enable the evaluation of the single-frequency (SF) approaches through comparison with the IntB-DF solution. This comparison is particularly robust because IntB-DF uses the Ka-band mean Doppler velocity, $\mathrm{V_M^{Ka}}$, which is generally less affected by aliasing, as the first guess for dealiasing the W-band observations and therefore does not rely on the continuity assumptions employed by SF approaches. DF-DCR of these characteristics can currently be found only in few sites in Europe at present, making this dataset particularly valuable for evaluating dealiasing performance across contrasting cloud conditions. Consequently, differences in algorithm performance can be largely attributed to atmospheric conditions rather than instrumental effects.

Data collected on 01 August 2024 at JOYCE and on 29 August 2024 at AGORA are used to assess RADALIA. The dataset represents two cloud regimes with distinct levels of dealiasing complexity. The first dataset was chosen to illustrate a scenario in

https://doi.org/10.5194/egusphere-2026-5139
Preprint. Discussion started: 9 September 2026

which dealiasing is straightforward, characterized by relatively smooth variations in the DVS shape with height. In contrast, the second dataset represents a more challenging case, including a more complex cloud structure with sharp DVS shape transitions due to different hydrometeor populations, faster movements, and strong attenuation. It was selected to explore the limitations and robustness of the different algorithm approaches.

2.1 NEBULA and JOYDURADO

The RPG-FMCW 35/94 dual-frequency Doppler cloud radars, NEBULA and JOYDURADO, are state-of-the-art cloud radars operating in the Simultaneous Transmission and Simultaneous Reception mode (STSR). In this mode, horizontally and vertically polarized signals are transmitted simultaneously, providing full polarimetric variables at both bands (Krasnov et al., 2023). Additionally, W and Ka-band antennas (beam widths are 0.56° and 0.84°, respectively) measure approximately the same volume, avoiding the problem of mismatching sampling volumes when using different radars as reported in previous studies (Tetoni et al., 2022). This is crucial because the dealiasing assessment of SF approaches relies on IntB-DF dealiased spectra, as aforementioned. For the analyzed period, NEBULA and JOYDURADO DVS data are filtered for power values below 6 times the standard deviation of the mean noise floor (Hildebrand and Sekhon, 1974). Both radars have the same setup and data resolution as summarized in Table 1, together with relevant technical specifications.

https://doi.org/10.5194/egusphere-2026-5139
Preprint. Discussion started: 9 September 2026

Table 1. NEBULA and JOYDURADO technical specifications.

Parameters		**W-Band**			**Ka-band**	
Transmitter Power (W)		10			1.5	
Beam Width [°]		0.56			0.84	
Operational Mode		STSR			Same	
Transmitter Frequency [GHz]		94			35	
	Chirp 1	**Chirp 2**	**Chirp 3**	**Chirp 1**	**Chirp 2**	**Chirp 3**
Range [m]	**100–600**	**600–2000**	**2000–12000**	**100–600**	**600–2000**	**2000–12000**
Range Resolution [m]	25.6	26.5	37.7		Same	
Total Bandwidth [MHz]	44.40	13.09	7.60		Same	
Sub-chirp Bandwidth [MHz]	5.86	5.66	3.98		Same	
Chirp Repetitions [#]	7168	7168	9216		Same	
Chirp Duration [µs]	84.57	103.49	170.79		Same	
Nyquist Frequency [kHz]	5.91	4.83	2.93		Same	
Nyquist Velocity [m/s]	9.43	7.71	4.67	25.34	20.71	12.55
Doppler FFT size	512	512	512		Same	
Total Time [s]	0.61	0.74	1.57		Same	

3 FMCW Doppler Cloud radars basis and aliasing effect

FMCW Doppler cloud radars transmit a continuous wave function linearly in the time-frequency space during a certain time, named chirp duration (t_Σ). In this space, the transmitted frequency (f_t) forms a "sawtooth" pattern referred as a chirp sequence. The slope of this sawtooth in the time-frequency space is related with the range resolution at each chirp sequence (Küchler et al., 2017). Different range resolutions per chirp can be configured in the RPG DCRs hardware settings, and the specific configurations used in this study are provided in Table 1. After a delayed time τ, the radar receives a backscattered echo with an additional phase shift for each moving particles in the sampled volume. This is the Doppler-induced phase shift $\delta\phi_{\mathrm{D}}(\mathrm{t})$ and it is associated with the scattered power of each particle. The power measured by the radar in the STSR mode is the co-polarized DVS component sB_{cc} (Myagkov et al., 2016). This component has the total combined H and V polarization power scattered by the radar volume and is used to compute the spectral moments. $\delta\phi_{\mathrm{D}}(\mathrm{t})$ can be expressed in terms of the Doppler frequency shift $\mathrm{f}_{\mathrm{D}}(\mathrm{t})$ using equation 1, and in terms of the Doppler velocity $\mathrm{V}_{\mathrm{D}}(\mathrm{t})$ from Doppler theory using equation 2, as follows:

https://doi.org/10.5194/egusphere-2026-5139
Preprint. Discussion started: 9 September 2026

$$f_D(t) = \frac{\delta\phi_D(t)}{2\pi t} \tag{1}$$

$$V_D(t) = \frac{cf_D}{2f_t} \tag{2}$$

where c is the speed of light, and f_t is the transmitted frequency. The scattered power in terms of $\mathrm{V_D(t)}$ is the DVS, and it is represented in Fig. 1a for all range gates. Note that $\delta\phi_\mathrm{D}(\mathrm{t})$ cannot be unambiguously interpreted for phase shifts outside the interval [-π, π], since any $\delta\phi_D(t) > 2\pi$ is mapped back into the same interval. Then, within a chirp sequence, the inequality $2\pi f_D t_\Sigma \leq \pi$ should be respected in order to avoid ambiguous measurements. As a result, when $\delta\phi_D(t) \rightarrow \pi$, the maximum unambiguous Doppler frequency shift $\mathrm{f_{Dm}}$ (the Nyquist frequency) is described by equation 3, and the maximum unambiguous Doppler velocity $\mathrm{V_N}$ (the Nyquist velocity) is described by equation 4. Aliasing occurs whenever the Doppler velocity $\mathrm{V_D(t)}$ of moving particles is either smaller than $-V_N$ or larger than $+V_N$.

$$f_{Dm} = \lim_{\delta\phi_D \rightarrow \pi} f_D(t = t_\Sigma) = \frac{1}{2t_\Sigma} \tag{3}$$

$$V_N = \lim_{\delta\phi_D \rightarrow \pi} V_D(t = t_\Sigma) = \frac{c}{4f_t t_\Sigma} \tag{4}$$

For NEBULA and JOYDURADO, a total chirp duration of $t_\Sigma = 103.49\,\mu$s yields $\mathrm{V_N}$ of 7.71 m s^{-1} at W-band, and 20.71 m s^{-1} at Ka-band (Tab. 1). Thus, the W-band is more prone to aliasing. Additionally, as indicated above, each band has different chirps at different range layers, meaning that the aliasing effect varies with height and becomes stronger at higher levels according to the settings described in Table 1.

In order to illustrate aliasing and the different spectral features to consider when addressing its correction, Fig. 1a displays a case of aliasing measured with the W-NEBULA (i.e., NEBULA measurements at 94 GHz) on 29 August 2024, during a rainfall event at 08:00 UTC. This figure shows the sB_{cc} in terms of $\mathrm{V_D}$ for each range gate, where the intensity of the power is given by the color scale. Each chirp is labeled in the figure and easily identified by its $\pm\mathrm{V_N}$ range (gray dashed lines, see values in Tab. 1). Aliasing is present in all chirp sequences in Fig. 1a. Although the effect becomes more severe in the third chirp because of its lower Nyquist velocity, the second chirp is highlighted with a red shadow and is used to represent the phenomenon. In this chirp, aliasing occurs in all range gates and is readily identifiable, since the resulting positive Doppler velocities are not physically consistent with a rainfall event. For the sake of clarity, Fig. 1b shows the spectrum at 1139 m (chirp 2) where the spectrum appears split into two regions, being the blue shaded area the aliased one, i.e. shifted by $+2V_N$ from its true position. The dealiased DVS is shown in Fig. 1c, where it can be seen that vertical velocities reach values near to -10 m/s. This correction has a significant impact on the spectral moments, i.e., $\mathrm{V_M}$, S_w, S_skew, and S_kurt. The original moments extracted from Fig. 1b are -0.97 m s^{-1}, 5.05 m s^{-1}, 0.51, and 1.68, respectively. However, after dealiasing (Fig. 1c), the corresponding values become -5.91 m s^{-1}, 2.87 m s^{-1}, 0.12, and 1.59, respectively. Therefore, dealiasing aims to provide accurate estimates of the Doppler moments while preserving the full information content of the Doppler velocity spectra.

In general, dealiasing consists of determining the integer n, which represents the number of $2V_N$ intervals by which a given portion of the Doppler velocity spectrum has been shifted due to aliasing. Once n is known, the true velocity can be recovered

https://doi.org/10.5194/egusphere-2026-5139
Preprint. Discussion started: 9 September 2026

from:

$$V_D = V_t + n2V_N \tag{5}$$

where $\mathrm{V_D}$ is the measured Doppler velocity, V_t is the true Doppler velocity, and $n = 0, \pm1, \pm2, \pm3$. Since V_t is unknown, the automatic determination of the value of n and which side of the spectrum must be shifted is not straightforward. Thus, an estimate of the true velocity, $\mathrm{V_G}$ is required. The accuracy of the dealiasing process therefore depends on the accuracy of $\mathrm{V_G}$, with larger errors increasing the likelihood of miscorrections. Once n is determined, the aliased spectrum can be corrected by shifting the folded part by $n2V_N/\Delta V_D$ offsets, where $\Delta\mathrm{V_D}$ is the DVS bin size (i.e., Doppler velocity resolution). However, an accurate determination of n is challenging, especially when it is equal or greater than 2 (Maahn and Kollias, 2012). In this scenario, $\mathrm{V_t}$ from another source (such as a second radar with a larger V_N), or alternatively, range and time continuity assumption as used in weather radars (Bergen and Albers, 1988; James and Houze, 2001), might improve the determination of n.

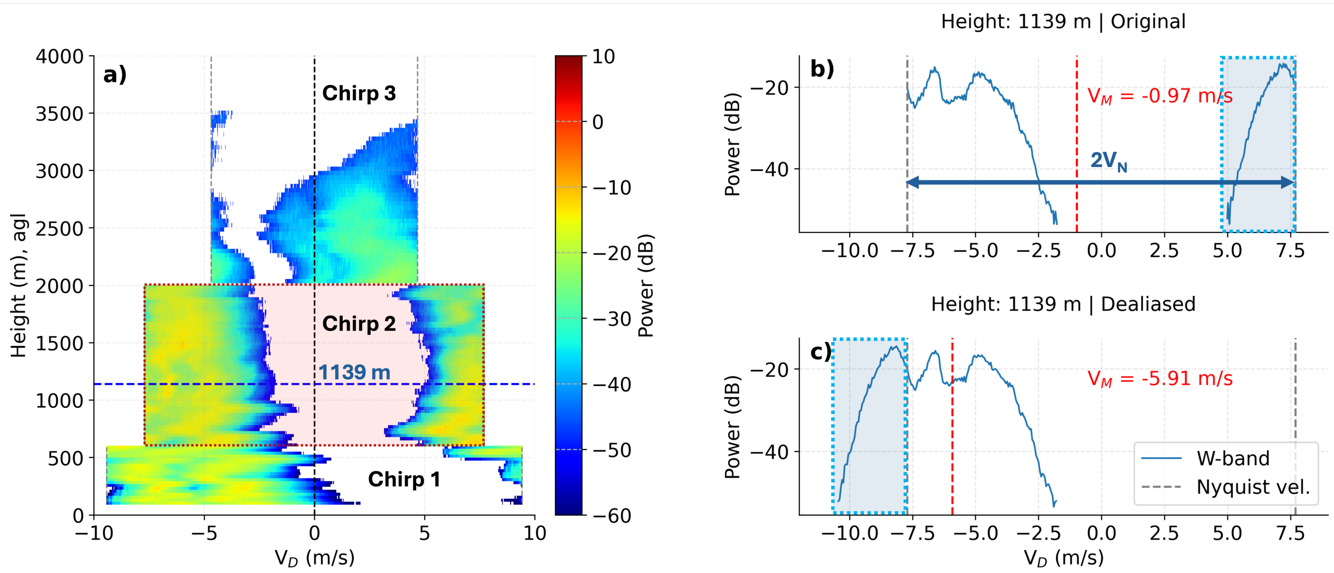

Figure 1. Doppler velocity spectrograms: (a) vertical spectrogram measured on 29 August 2024 at 08:00 UTC using the chirp configuration shown in Table 1. V_N is denoted by gray dashed lines and aliasing at the second chirp is highlighted by the red shaded area. The blue dashed line indicates the spectrum location shown in (b); (b) aliased DVS at 1139 m (light blue line), and V_M (dashed red line and value in red) is shown. The blue shaded box indicates which part of the spectrum was shifted due to aliasing; (c) dealiased DVS, with its dealiased V_M (red)

https://doi.org/10.5194/egusphere-2026-5139
Preprint. Discussion started: 9 September 2026

4 Methods

4.1 RADALIA tool

RADALIA is a tool which focuses on dealiasing sB_{cc} by obtaining an accurate estimation of $\mathrm{V_G}$ and n, through two different methods: an interpolation based method (IntB) and an iterative bottom-up method (IterBU) (see workflow in Fig. 2). The IntB includes a pre-processing of the data enhancing their quality prior to dealiasing and $\mathrm{V_G}$ can be obtained using two different sources. On the other hand, the IterBU offers a straightforward self-contained solution, without pre-processing. A compromise between both approaches introduces balance between adaptability and computational efficiency. While the IntB approach allows the user to tune the pre-processing parameters to improve the dealiasing performance under specific observational conditions, the IterBU method provides a more automatic and computationally lightweight solution. As presented in Fig. 2, the input of both methods is the sB_{cc} from RPG level 0 binary files. Once introduced in RADALIA, these input files are processed according to one of the two methods, and a dealiased sB_{cc} is provided as output. The detailed workflow for both methods is presented next.

https://doi.org/10.5194/egusphere-2026-5139
Preprint. Discussion started: 9 September 2026

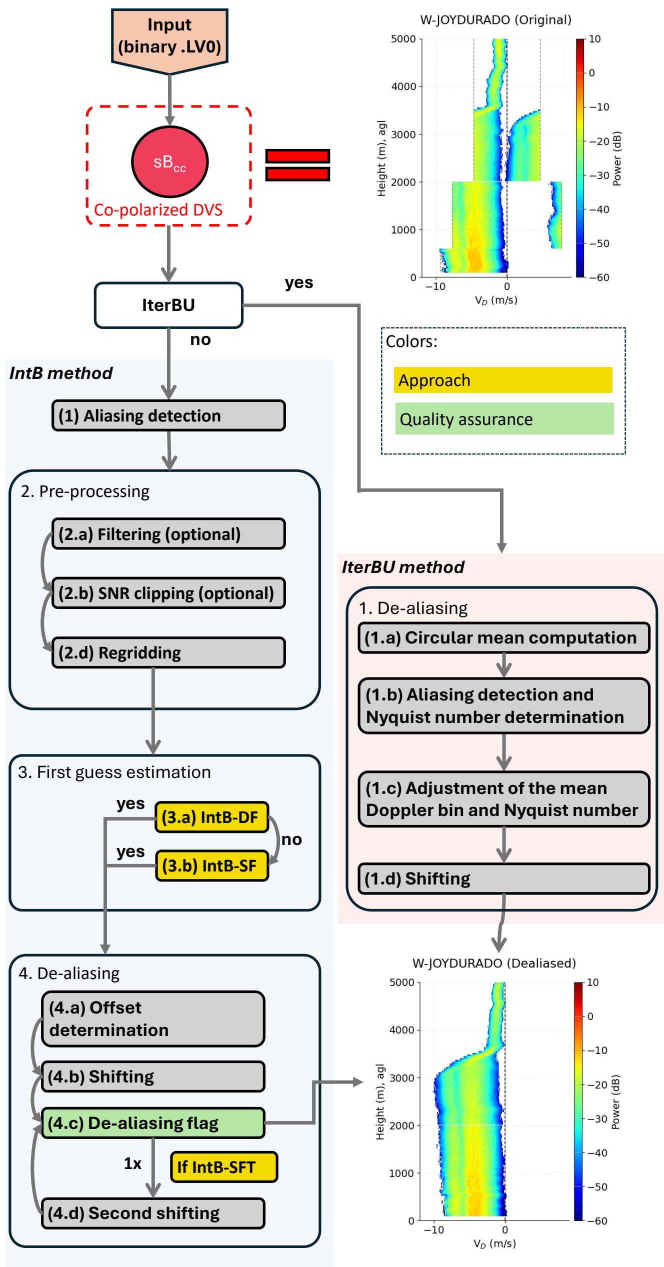

Figure 2. Diagram of RADALIA workflow. It shows the processing steps of IntB and IterBU dealiasing approaches.

4.1.1 IntB workflow

The IntB method tackles the dealiasing in four modules: (1) aliasing detection module: detect aliasing in order to determine which profile must be dealiased and which range gates can be used to estimate V_G in SF approaches included in this method,

https://doi.org/10.5194/egusphere-2026-5139
Preprint. Discussion started: 9 September 2026

(2) the pre-processing module: aims for reducing the effect of artifacts and facilitate data handling between chirp sequences, (3) the V_G estimator module: considers two options for finding V_G, and (4) the dealiasing module: corrects aliasing as illustrated in Fig. 3. These modules are described as follows:

1. *Aliasing detection*. DVS is flagged at each range gate when the number of bins containing data in both left and right ends of the spectrum exceeds a defined threshold. By default, the last 5 bins on the left and right edges are checked, but this value can be user-defined. When using the dual-frequency approach, an aliasing mask is also computed for the Ka-band in order to identify reliable range gates used for dealiasing the W-band. In any case, when the aliased spectrum may no longer contain signal at the Nyquist interval, it cannot be detected. In these cases aliasing cannot be detected without extra information, such as the Ka-band spectrum. This is more likely in cases of small V_N and fast-moving targets, increasing the aliasing detection uncertainty since it cannot catch aliasing present in the neighborhood of flagged range gates. Therefore, users who are not interested in these regions for their specific application may simply exclude flagged range gates and a surrounding margin of approximately ±500 m, rather than applying a dealiasing algorithm.

2. *Pre-processing*

   (a) *Filtering (optional).* DVS with less than a minimum fraction of non-empty velocity bins (i.e., fraction threshold) are discarded. By default, the fraction threshold is 10%. This filtering step ensures that only spectra with a sufficient number of valid observations are retained, reducing the influence of artifacts and noise-dominated measurements.

   (b) *SNR clipping (optional).* By default, no clipping is applied, but DVS with signal-to-noise ratio (SNR) below a chosen threshold might be removed and this SNR threshold can be adjusted. To apply this clipping, it is important to consider that large thresholds may remove data at the edges of the spectrum, complicating folding detection, while low thresholds may retain spurious speckles. This step ensures that DVS are mainly influenced by hydrometeors, not noise, and it complements the noise removal of Hildebrand and Sekhon (1974), already applied by the radar software.

   (c) *Regridding.* This step creates a new Nyquist interval to account for the different spectral resolutions associated with each chirp configuration. The regridding facilitates data handling between chirps with different ΔV_D. In this step, each DVS within a chirp sequence is resampled onto a common velocity grid ranging between $\pm\, 1.8\, V_{N,max}$ across chirps, with $V_{N,max}$ being the maximum V_N of the different chirps. A new Doppler velocity resolution ΔV_D is applied. By default, a resolution of 0.1 m s^{-1} is used, although this parameter can be modified by the user.

3. *First guess estimation*. A reliable estimation of V_G is essential for the dealiasing process. Within the IntB workflow, two possible strategies are considered: (i) using an external estimate of V_G as a reference (IntB-DF); (ii) relying on stand-alone measurements when no external reference track is available (IntB-SF), with a secondary correction constraining V_G through a temporal-stability assumption on the air motion. This secondary correction is optional and is interpreted as an additional refinement of IntB-SF, named IntB-SFT. Further details on each option are provided below:

https://doi.org/10.5194/egusphere-2026-5139
Preprint. Discussion started: 9 September 2026

(a) *IntB-DF.* For dealiasing W-band data, $\mathrm{V_G}$ is obtained from $\mathrm{V_M^{Ka}}$ from the Ka-band collocated radar (if available). It is assumed that the frequency separation (94 and 35 GHz) is close enough to sample substantially similar hydrometeor populations; therefore, the W-band mean Doppler velocity $\mathrm{V_M^W}$ is expected to be practically the same for both bands in most cases.

(b) *IntB-SF.* Based on the *Aliasing detection* mask, at aliased range gates, $\mathrm{V_G}$ is set to $\mathrm{V_M}$ from the previous profile, provided it is reliable according to the *Dealiasing flag*. Since the current profile may contain undetected aliasing as discussed in the *Aliasing detection* step, $\mathrm{V_G}$ at unaliased range gates is calculated as the arithmetic mean of the current and previous profile values. This approach reduces the impact of undetected aliasing near aliased gates and provides estimates for missing data. If the previous profile is unreliable, $\mathrm{V_G}$ is derived via linear interpolation of $\mathrm{V_M}$ from unaliased range gates identified by the mask.

4. *Dealiasing*

(a) *Offset determination.* The sign of the Doppler velocity V_G determines the direction of the spectral shift. For $\mathrm{V_G} < 0$, the right portion of the DVS is shifted to the left-hand side, while the opposite applies for $\mathrm{V_G} > 0$ (Fig. 3a and 3b). As illustrated in Fig. 3a, the offset is determined as the number of Doppler velocity bins (resolution $\Delta\mathrm{V_D}$) by which the right portion of the DVS (blue shaded area) must be shifted to obtain a displacement of $2\mathrm{V_N}$ toward lower velocities. Then, all red bars within the blue area must be shifted by this offset.

In both figures, the DVS is divided into two portions by finding the discontinuity interval either as a gap in the DVS or, when the two portions are merged, as the spectral minimum.

i. If the Doppler velocity $\mathrm{V_G} < 0$, the right portion of the spectrum is shifted to the left side as shown in Fig. 3a.

ii. If the Doppler velocity $\mathrm{V_G} > 0$, the left portion of the DVS is shifted to the right side as shown in Fig. 3b.

(b) *Shifting.* The left or right portion of the spectrum is shifted according to the offset determined in the previous step (see Fig. 3), which dealiases the spectrum.

https://doi.org/10.5194/egusphere-2026-5139
Preprint. Discussion started: 9 September 2026

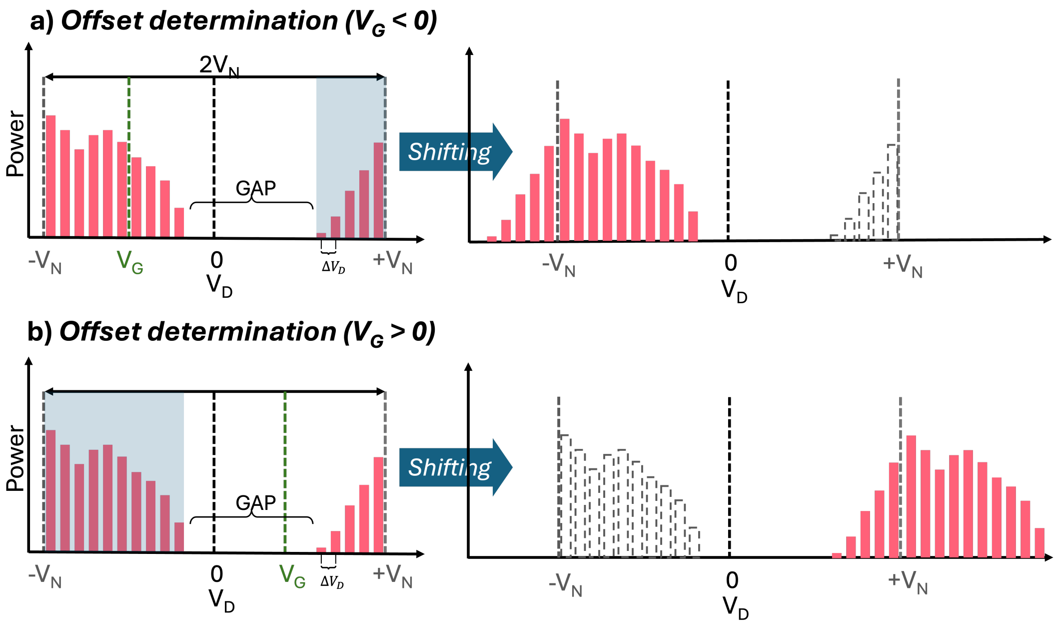

Figure 3. Illustration of the offset-determination procedure used by the IntB approach: (a) original and dealiased spectra for the case $V_G < 0$; (b) original and dealiased spectra for the case $V_G > 0$. The original spectrum, V_G, discontinuity interval, and ΔV_D are shown on the left, while the corresponding dealiased spectrum is shown on the right.

(c) *Dealiasing flag.* The dealiasing flag is a mask that classifies the quality of the dealiasing. It identifies: (i) No aliasing cases, where no correction is required, (ii) Dealiased range gates, where aliasing is present and the correction is considered reliable, and (iii) Suspicious range gates, where the correction is likely unreliable. Unreliable cases are detected by inspecting range discontinuities in the dealiased $\mathrm{V_M}$. Under the assumption that hydrometeor populations vary smoothly with range, strong vertical gradients are not expected. A threshold based on $\mathrm{V_N}$ (4.67, 7.71, and 9.43 m s^{-1} for each chirp; see Table 1) is applied between adjacent range gates. If $V_{M_z} - V_{M_{z-1}} > V_N$, where V_{M_z} and $V_{M_{z-1}}$ are the mean Doppler velocity at range gate z and $z-1$, respectively, the specific range gate is flagged as suspicious. Otherwise, it is considered reliable.

(d) *Second shifting.* When the optional IntB-SFT is selected, a second shifting is performed whether the current dealiased profile generated by IntB-SF have any range gate marked as "suspicious" by the Dealiasing flag. Since the temporal resolution is 3 s (see Table 1), significant changes in cloud microphysics are not expected between successive profiles. Therefore, $\mathrm{V_M}$ is assumed to remain approximately unchanged over consecutive profiles. Then, the previous $\mathrm{V_M}$ profile, either already dealiased or unaffected by aliasing, is used as a reference to dealias the current profile, thereby enforcing temporal continuity.

In case the previous profile was flagged as successfully dealiased, this profile is used as a new guess $\mathrm{V_{G_2}}$. Then, new offsets are determined by minimizing the difference between $\widetilde{\mathrm{V}}_\mathrm{M}$ and $\mathrm{V_{G_2}}$ in multiples of $2V_N$ (i.e., $n2V_N$,

https://doi.org/10.5194/egusphere-2026-5139
Preprint. Discussion started: 9 September 2026

where $n = 0, \pm 1, 2, 3$). Fig. 4a illustrates a wrong dealiased DVS due to a bad estimation of $\mathrm{V_G}$. Using the corrected previous profile as a new guess $\mathrm{V_{G_2}}$, it is possible to observe that for minimizing the distance between $\widetilde{\mathrm{V}}_\mathrm{M}$ and $\mathrm{V_{G_2}}$, n should be -1, and the new offsets are defined as $-2V_N/\Delta V_D$. Fig. 4b illustrates the new DVS (in red) after the second shifting.

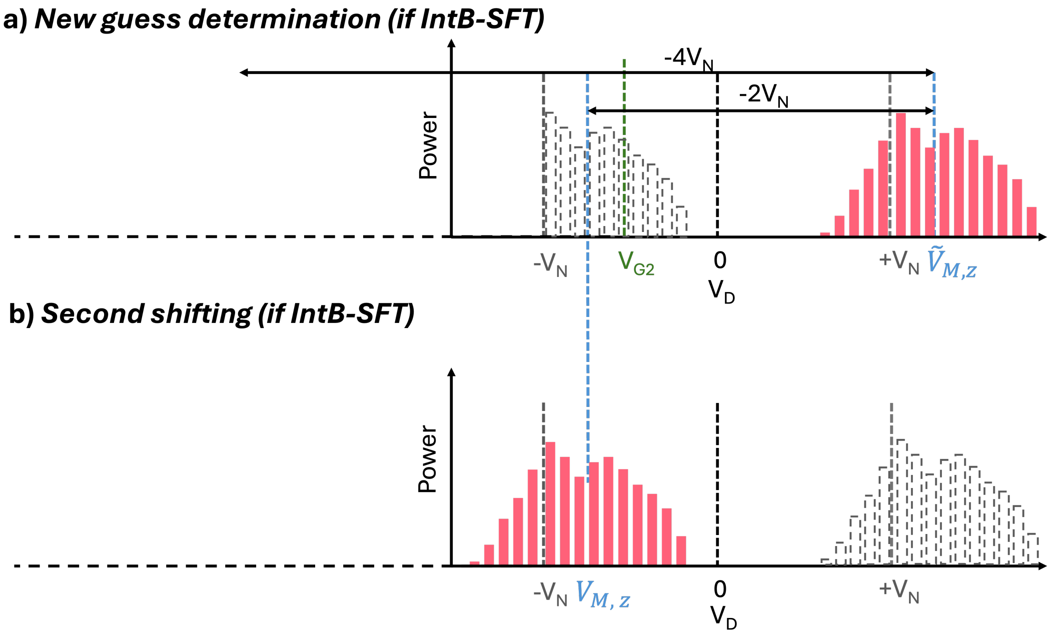

Figure 4. Illustration of the second shifting procedure used by IntB-SFT: (a) determination of the new first guess V_{G2} from a previously dealiased profile after an incorrect initial correction; (b) dealiased spectrum after applying the second shifting using the selected solution.

For this study, RADALIA was configured using the default options and no *SNR clipping* was applied to ensure a consistent comparison with IterBU using identical input spectra.

4.1.2 IterBU workflow

The IterBU method is a fully self-contained dealiasing approach that estimates the first guess by exploiting range continuity. The algorithm proceeds from the lowest range gates upward and assumes that microphysical properties do not change much between adjacent gates and therefore exhibit comparable $\mathrm{V_M}$. To account for the periodic nature of aliased spectra, the Doppler spectrum is first analyzed in a circular Doppler bin space. Therefore, sB_{cc} is expressed in terms of Doppler bins ($k = 1, 2 \ldots N$) rather than Doppler velocity bins (V_D). A preliminary dealiasing solution is obtained independently for each chirp and is subsequently refined using range continuity constraints. Finally, the spectra are shifted onto their dealiased velocity positions.

Conceptually, IterBU consists of four main steps: (a) estimation of the mean Doppler bin position in a circular domain, (b) identification and correction of Nyquist boundary crossings between adjacent range gates, (c) refinement of the solution using

https://doi.org/10.5194/egusphere-2026-5139
Preprint. Discussion started: 9 September 2026

range continuity, and (c) reconstruction of the dealiased Doppler spectrum through spectral shifting. The equivalent to the offset used by the IntB is referred here as the *Nyquist number*. It represents the integer number of Nyquist intervals by which a spectrum must be shifted to recover its dealiased position. The method consists of a single dealiasing module, illustrated in Fig. 2 and described in more details below.

1. Dealiasing

   (a) *Circular mean computation.* The Doppler spectrum is defined on a periodic velocity axis due to the Nyquist limit, such that the first and last Doppler bins are adjacent in velocity space. To account for this periodicity, V_M is estimated using a circular mean in the Doppler bin space. In this space, $S(k)$ denotes the spectral power at the bin k, with $k = 0, \ldots, N-1$, and N is the number of spectral bins. Each Doppler bin is mapped onto an angular coordinate on the unit circle according to $\theta_k = 2\pi k/N$. The weighted circular mean is obtained from the first trigonometric moments B$= \sum_{k=0}^{N-1} S(k)\sin(\theta_k)$ and C $= \sum_{k=0}^{N-1} S(k)\cos(\theta_k)$. The mean angle is then $\theta_m = \arctan(B, C)$, and the corresponding mean Doppler-bin position is

$$k_M = \theta_m N/(2\pi). \qquad (6)$$

   Because the Doppler axis is periodic, bins located at opposite ends of the spectrum correspond to neighboring positions on the unit circle. Therefore, spectral power distributed across the Nyquist boundaries still yields a physically meaningful estimate of k_M close to the spectral peak. This concept is illustrated in Fig. 5a, where the Doppler spectrum $S_z(k)$ is represented by the red bars on the unit circle.

   (b) *Aliasing detection and Nyquist number determination.*

   The Nyquist number is estimated by examining the continuity of the mean Doppler-bin position between adjacent range gates. Under normal atmospheric conditions, abrupt changes in hydrometeor fall velocity are not expected between neighboring gates. Therefore, large discontinuities in k_M are interpreted as spectral folding events rather than a normal atmospheric variability. The Nyquist interval associated with a given mean Doppler bin is defined as $[k_M - \frac{N}{2}, k_M + \frac{N}{2}]$. This interval is represented by the red point in Fig. 5b and corresponds to region I in Fig. 8a. The mean Doppler bin position from the previous range gate, $k_{M_{z-1}}$, is used as a first guess estimate and is denoted by k_G.

   Because the Doppler axis is periodic, a spectrum crossing a Nyquist boundary may appear as a sudden jump from one end of the Doppler domain to the other. Such discontinuities are identified when the difference between adjacent range gates approaches the total Doppler domain length N. Fig. 5b illustrates this situation by the black arrow. The following procedure is applied independently to each chirp:

      i. If $k_{M_z} - k_{M_{z-1}} < -0.75N$, the discontinuity is interpreted as a positive wraparound across the Nyquist boundary. A new representation is obtained by adding N to the current mean Doppler-bin position, $k^*_{M_z} = k_{M_z} + N$.

https://doi.org/10.5194/egusphere-2026-5139
Preprint. Discussion started: 9 September 2026

The corresponding Nyquist interval becomes $[k_{M_z} + \frac{N}{2}, k_{M_z} + \frac{3N}{2}]$. This situation is illustrated in Fig. 5c and by region II in Fig. 6a.

ii. If $k_{M_z} - k_{M_{z-1}} > 0.75N$, the discontinuity is interpreted as a negative wraparound. In this case, N is subtracted from both the mean Doppler-bin position and the associated Nyquist interval.

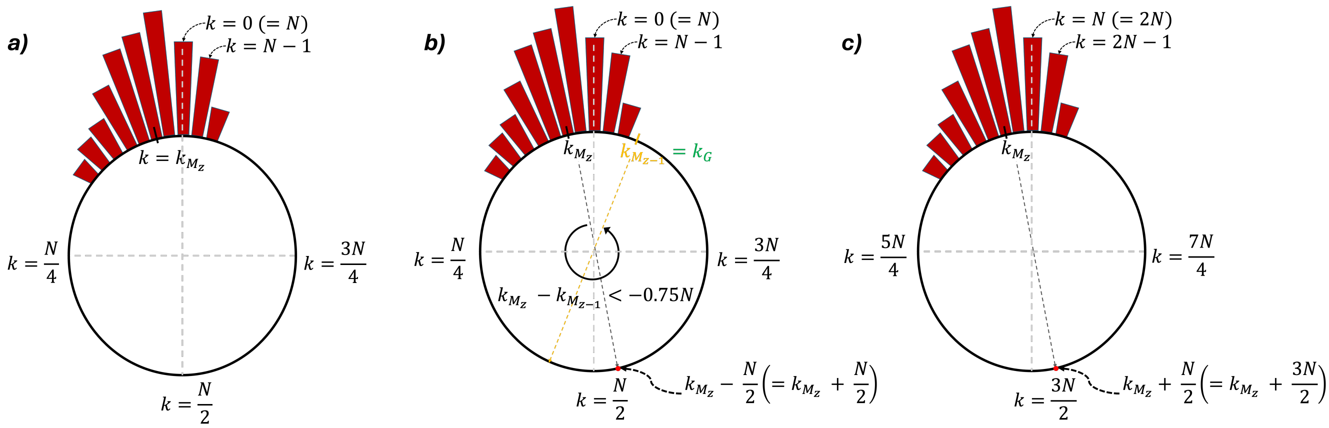

Figure 5. Illustration of the IterBU procedure in circular Doppler-bin space: (a) Doppler spectrum $S_z(k)$ represented on the unit circle; (b) the same as (a), indicating the original Nyquist interval, mean Doppler-bin position from the previous range gate $k_{M,z-1}$, and aliasing conditions; (c) updated Nyquist interval after aliasing correction (red point).

(c) *Adjustment of the mean Doppler bin and Nyquist number.*

The preliminary solution obtained in the previous step may still be ambiguous because multiple periodic representations of the same spectrum are mathematically possible. Therefore, a second continuity constraint is applied to refine the solution. The chirp sequences are processed from lower toward higher altitudes, assuming that the lowest gates are either unaliased or have already been correctly dealiased. Furthermore, the method assumes that the dominant hydrometeor population evolves gradually between adjacent range gates. The dealiased mean Doppler-bin position from the previous gate is used as a new guess estimate, $k_{G_2} = k_{M_{z-1}}$. A set of possible periodic representations of the current spectrum are then examined, $k_{M_z} + nN$, where $n = 0, \pm 1, \pm 2, \ldots$.

The representation that minimizes the distance to k_{G2} is selected as the final solution. As illustrated in Fig. 6b, the candidate $k_{M,z} + 2N$ provides the smallest separation from the reference estimate and is therefore chosen. The associated Nyquist interval is shifted accordingly, becoming $[k_{M_z} + 3N/2, k_{M_z} + 5N/2]$. The resulting mean Doppler-bin position and Nyquist interval define the final dealiased solution for the current range gate.

(d) *Shifting.* Finally, the Doppler spectrum $S(k)$ is circularly shifted according to the dealiased mean Doppler bin position and Nyquist interval obtained in the previous step. This operation relocates the spectral power to its dealiased position within the Doppler domain. Since different range gates may require different shifts, all spectra are projected onto an expanded Doppler grid whose limits are determined by the minimum and maximum dealiased

https://doi.org/10.5194/egusphere-2026-5139
Preprint. Discussion started: 9 September 2026

Nyquist intervals within each chirp sequence. Each shifted spectrum is inserted into this common grid according to its corresponding dealiased Nyquist interval. The Doppler-bin coordinates are subsequently converted into Doppler velocity coordinates, yielding the final dealiased Doppler velocity spectrum (DVS).

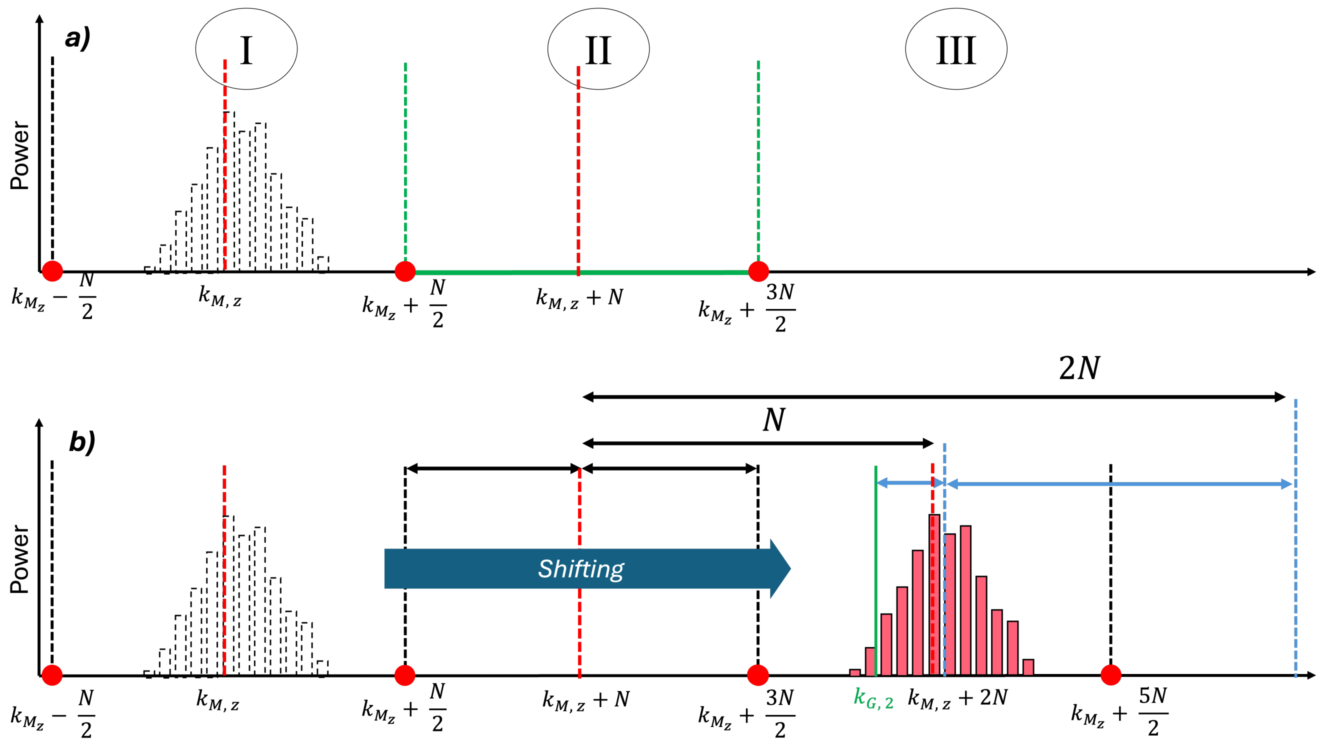

Figure 6. Illustration of the IterBU dealiasing procedure on a linear Doppler-bin space: (a) original spectrum in region I (white histogram with dashed edges), and the dealiased mean Doppler-bin position and associated Nyquist interval (green) in region II; (b) continuity-based refinement step using the reference estimate k_{G2}. The resulting dealiased spectrum is shown in region III.

5 Assessment of RADALIA's dealiasing methods

This section presents the assessment of RADALIA by means of detailed inspections of individual Doppler spectrograms and extended observation through a 1-hour DCR measurement. In both analysis, data from two observational sites with different atmospheric conditions, JOYCE and AGORA stations, are used.

5.1 Assessment of dealiased spectrograms

The first case study was observed at the JOYCE station on 01 August 2024 at 08:25 UTC. Fig. 7a shows the original JOYDU-RADO W-band spectrogram, Fig. 7b shows the corresponding Ka-band spectrogram, and Fig. 7c shows the W-band de-aliased spectrogram produced by IntB-DF. The $\mathrm{V_M}$ profile of each spectra is also indicated in each figure by $\mathrm{V_M^W}$ (blue), $\mathrm{V_M^{Ka}}$ (gray),

https://doi.org/10.5194/egusphere-2026-5139
Preprint. Discussion started: 9 September 2026

and V_M^{De} (green), respectively. As shown in Fig. 7a, the W-band spectrum in region C1 exhibits no aliasing, with two peaks indicated by yellowish tones. It suggest the presence of two hydrometeor populations separated by resonance effects resulting from Mie scattering. In contrast, the Ka-band spectrum (Fig. 7b) exhibits only one peak, consistent with scattering in the Rayleigh regime. Region C2 also displays a bimodal spectrum, although aliasing is present. Due to the aliasing in the W-band, the discrepancy between V_M^W and V_M^{Ka} increases compared to C1. In region C3a, aliasing is particularly severe due to the low value of V_N, while a sudden increase in V_M^W at the beginning of the third chirp also causes a substantial difference with V_M^{Ka}. In region C3b, aliasing continues but is less pronounced owing to the lower measured velocities. Furthermore, the bimodal structure is no longer visible in the W-band spectrum, indicating the same scattering regime for both bands. The Ka-band spectrum shown in Fig. 7b is used as a reference in this study, but note that the Ka-band spectra sometimes exhibit a ghost echo in the third chirp, which is a detached spurious spectral artefact with positive Doppler velocity above 2 km, likely caused by instrumental effects. Additionally, the first 600 m are affected by near-range instrumental contamination, appearing as a broadband enhancement across much of the Doppler spectrum. However, these artifacts do not affect the dealiasing itself and are expected to have an impact only under low-SNR conditions, as shown in the next section. In any case, near-range instrumental contamination can be identified using the Ka-band aliasing mask and effectively filtered out. The ghost echoes typically exhibit much lower signal levels than cloud hydrometeors and therefore do not affect the dealiasing.

As shown in Fig. 7c, the original spectrogram is correctly dealiased by IntB-DF approach since the final DVS matches the Ka-band spectrum shape (Fig. 7b), and V_M^{De} is proportional to V_M^{Ka}. It is a strong indicator of successful dealiasing since both bands are expected to observe similar DVS. In this case, the correction performs smoothly, with no significant discontinuities, and all approaches (i.e., IterBU, IntB-DF, IntB-SF, and IntB-SFT) yield identical results. Note that the approaches work even in region C3a, where the signal starts to overlap. Once a global minimum can be clearly identified, all methods must still perform well.

https://doi.org/10.5194/egusphere-2026-5139
Preprint. Discussion started: 9 September 2026

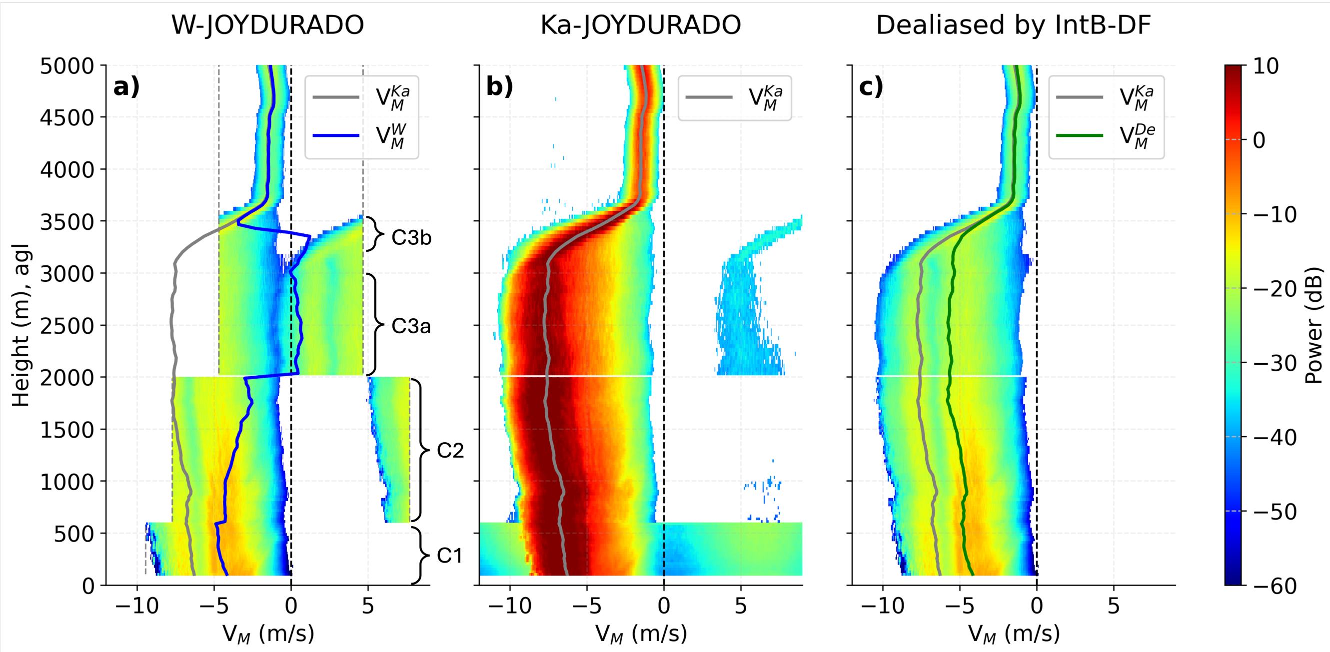

Figure 7. Doppler velocity spectrograms observed at the JOYCE station on 01 August 2024 at 08:25 UTC: (a) original W-band spectrogram from JOYDURADO; (b) corresponding Ka-band spectrogram; (c) W-band spectrogram dealiased using IntB-DF. Mean Doppler velocity profiles are shown in blue (W band), gray (Ka band), and green (dealiased W band). C1, C2 C3, and C3b are subsections of each chirp sequence defined in Tab. 1. No additional dealiasing approaches are shown because they produced the same result.

A more detailed inspection of the spectrum in regions C1, C3a, and C3b are illustrated in Fig. 8a, b, and c, respectively. These figures display the DVS for the original W-band (blue), the original Ka-band (grey), and the dealiased W-band (green) at 874, 2297 and 3427 m of height, respectively. At 874 m (Fig. 8a), two hydrometeor populations are detected at the W-band, and the first Mie notch is visible, separating the two peaks. Although the W-band operates in the Mie regime and the Ka-band in the Rayleigh regime, their S_w are similar (1.40 m s^{-1} for the W-band and 1.02 m s^{-1} for the Ka-band). Therefore, $\mathrm{V_M^{Ka}}$ remains an accurate proxy for $\mathrm{V_G}$. Fig. 8b shows the DVS's at 2287 m, where the severe aliasing causes the overlap of the Doppler spectra. Nevertheless, a well defined global minimum can be identified, and this minimum is subsequently used as the reference point to partition the spectrum, after which the aliased portions are shifted to their correct velocity positions. The clear identification of this minimum ensures a robust reconstruction of the spectrum despite the strong aliasing effects. At an height of 3427 m (Fig. 8c), the W-band signal is strongly attenuated, yet only a single spectral mode is present. Under these conditions, $V_{\mathrm{M}}^{\mathrm{Ka}}$ provides a very accurate estimate of $\mathrm{V_G}$ because both bands have the same DVS shape.

https://doi.org/10.5194/egusphere-2026-5139
Preprint. Discussion started: 9 September 2026

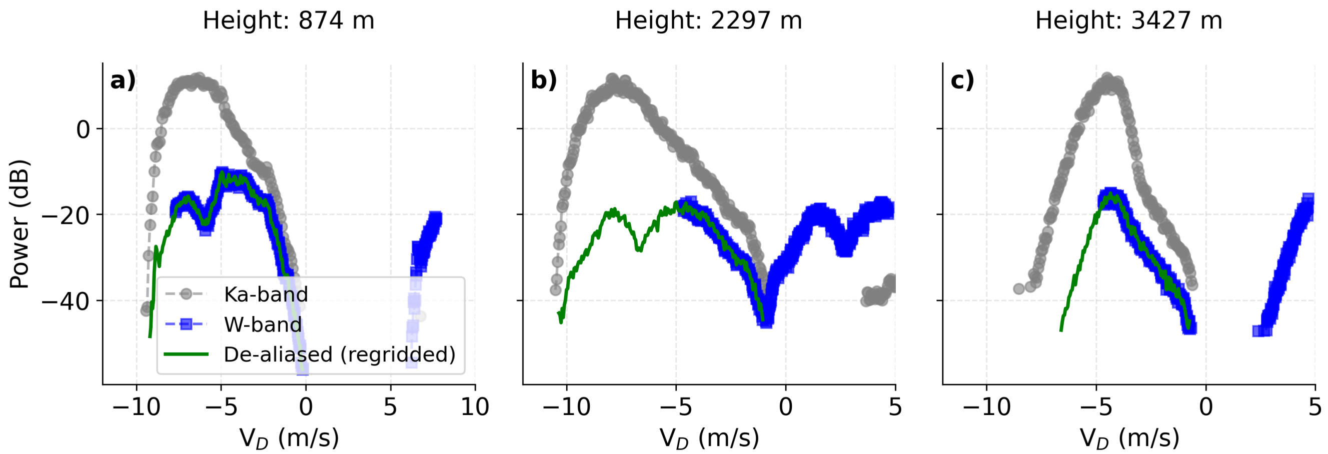

Figure 8. Doppler velocity spectra corresponding to regions C2, C3a, and C3b in Fig. 7, respectively: (a) spectrum at 874 m; (b) spectrum at 2297 m; (c) spectrum at 3427 m. The original W-band spectrum is shown in blue, the original Ka-band spectrum in gray, and the dealiased W-band spectrum in green. Note that the dealiased spectra were regridded as part of the IntB processing. Therefore, their Doppler velocity resolution differs from that of the original spectra.

The second case study, observed at the AGORA station on 29 August 2024 at 00:45 UTC, is discussed due to its complex spectra since (i) multiple hydrometeor populations can be identified, ii) aliasing cannot be detected in some range gate intervals, and iii) the W-band and Ka-band radars sampled different hydrometeor populations. As shown in Fig. 9a, region C1 does not present aliasing, while region C2a exhibits a weak aliasing, which has a negligible impact on the spectral interpretation. Region C3a exhibits severe aliasing that cannot be identified due to a lack of data at the spectrum's edges. In region C3b, aliasing is then detected.

The Ka-band reference is shown Fig. 9b, and the dealiased W-NEBULA spectrogram using IntB-SF, IntB-SFT, IterBU, and IntB-DF are shown in Fig. 9c, d, e, and f, respectively, where V_M profiles are omitted here for clarity. Differences between dealised W-band and the Ka-band spectrograms (uncorrected dealiasing) are highlighted in yellow in Fig. 9c–f and discussed below:

https://doi.org/10.5194/egusphere-2026-5139
Preprint. Discussion started: 9 September 2026

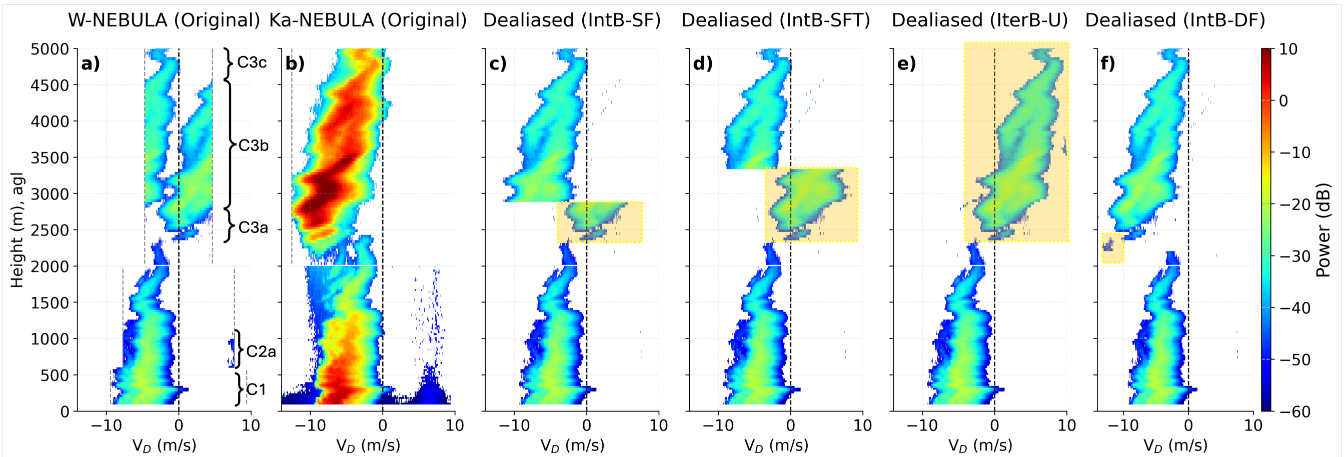

Figure 9. Doppler velocity spectrograms observed at the AGORA station on 29 August 2024 at 00:45 UTC: (a) original W-band spectrogram from NEBULA; (b) corresponding Ka-band spectrogram; (c) W-band spectrogram dealiased using IntB-SF; (d) W-band spectrogram dealiased using IntB-SFT; (e) W-band spectrogram dealiased using IterBU; (f) W-band spectrogram dealiased using IntB-DF. The undetected aliasing region (C3a), detected aliasing region (C3b), and regions of incorrect dealiasing are highlighted in yellow and discussed in the text.

- *IntB-SF*: almost the entire spectrogram was correctly dealiased, except for the part where no aliasing was detected in C3a and some surrounding range gates above it, as can be seen in Fig. 9c. The $\mathrm{V_M^W}$ values in C3a and C3c were used as reference and interpolated within C3b for use as $\mathrm{V_G}$ in aliased range gates, resulting in incorrect dealiasing, as shown in the yellow area of Fig. 9c.

- *IntB-SFT*: most part of the spectrogram was correctly dealiased, but the uncorrected region increased compared with *IntB-SF*, as shown in Fig. 9d. The previously dealiased profile was inaccurately corrected but flagged as reliable. Consequently, this profile was used as new guess $\mathrm{V_{G_2}}$, which is unsuitable for correcting the current spectrogram. Therefore, for highly complex spectrograms, as the one presented here, dealiasing flagging issues may lead to propagate errors in time, as the one indicated by the yellow area in Fig. 9d. For less complex spectra, the *Dealiasing Flag* is accurate, and temporal continuity constraints may provide additional benefit when aliased regions extend over larger continuous regions of range gates and when IntB-SF fails.

- *IterBU*: above 2.4 km, the spectrogram is incorrectly dealiased. When moving from the lower part of the spectra to the upper one, around 2.4 km, an incorrect aliasing detection is propagating towards the top of the cloud. The method uses the $\mathrm{V_M}$ from the lower gate as $\mathrm{V_G}$, causing the subsequent gate to be pulled toward this value. This bias then propagates upward, affecting the entire profile up to cloud top. In this case, the assumption of no significant changes in microphysics between consecutive range rates is violated, propagating the error up to the cloud top, as can be seen in Fig. 9e by the yellow area.

https://doi.org/10.5194/egusphere-2026-5139
Preprint. Discussion started: 9 September 2026

– *IntB-DF*: this approach yields the most effective results, almost perfectly dealiasing the entire profile, except for a minor issue in the indicated yellow region in Fig. 9f. For this region, the Ka-NEBULA detected multiple hydrometeor populations while the W-NEBULA detects only a single peak, violating the assumption that both bands are observing the same particle population. This is due to higher sensibility of the Ka-band to detect large particles compared to the the W-band. To illustrate this behavior, a detailed view of the Ka and W band spectrum at 2222 m is shown in Fig. 10a, where $\mathrm{V_M^{Ka}}$ is closer to larger particle peaks on the right. When this velocity is used as $\mathrm{V_{G_2}}$, the dealiasing algorithm shifts the W-band peak associated with smaller particles, originally close to 0 m $\mathrm{s^{-1}}$, toward the large-particle peaks detected by the Ka-band. Above this level, only a single mode is observed by both frequencies, where the W-band spectrum is consistently shifted toward the corresponding Ka-band peak, as can be seen for the example at 2674 m in Fig. 10b. However, the benefit of this method is that $\mathrm{V_G}$ is independent of the aliasing detection, which affected the other approaches. It is worth noting that Fig. 10b shows the dealiased W-band spectrum at 2674 m matching the Ka-band spectrum, even though no aliasing was detected. This highlights the robustness of this approach, which only fails when the Ka-band detects larger particles undetected by the W-band due to sensitivity limitations.

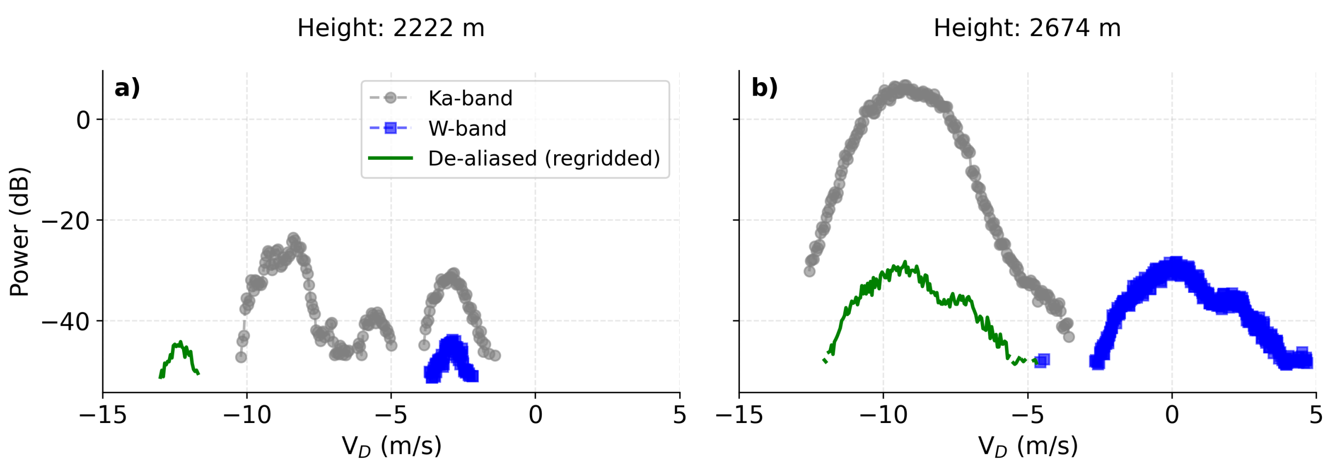

Figure 10. Same as Fig. 8, but for spectra at the AGORA station shown in Fig. 9: (a) spectrum at 2222 m; (b) spectrum at 2674 m.

The two case studies show that the proposed approaches effectively dealiased most of the DVS's. While all approaches performed fairly well in the straightforward case, differences were observed for the more complex spectra. The IterBU and IntB-SFT were more prone to error propagation, whereas the IntB-DF provided the most effective approach, correctly dealiasing almost the entire spectrogram in the challenging case. The primary sources of error were incorrect aliasing detection and incorrect identification of artifacts (i.e., provided by the *Dealiasing flag*). Strong aliasing can remain undetected when there is no spectral power at the DVS's edges, thereby decreasing the performance of all approaches, except IntB-DF. Nevertheless, such situations are rare and usually occur only under extreme conditions. Additionally, DVS's near range gates with detected aliasing should be interpreted with caution due to the consistent presence of unflagged aliased spectra in these areas.

https://doi.org/10.5194/egusphere-2026-5139
Preprint. Discussion started: 9 September 2026

5.2 Dealiasing performance on continuous measurements

The temporal consistency of RADALIA is assessed for different spectrogram scenarios observed with W-JOYDURADO between 08:00 and 09:00 UTC on 1 August 2024. As it can be seen in Fig. 11a, the original $\mathrm{V_M^W}$ shows an unrealistic sharp shift at 2 km between second and third chirps (see Tab. 1), indicating strong aliasing, at least in the lowermost part of the third chirp due to its smaller $\mathrm{V_N}$ (from -4.67 to $+4.67$ m s^{-1}). The aliasing mask, showed in Fig. 11b, confirms that aliasing is also present in the second chirp (between 0.6 and 2 km) and occasionally in the first chirp, presenting an homogeneous pattern almost concentrated in one height interval. The *Dealiasing flag* shown in Fig. 11c indicates reliable and unreliable (i.e., the algorithm may have introduced artifacts) dealiasing by "Dealiased" and "Suspicious" pixel, respectively. "Suspicious" pixels are hardly identified in the whole time series; thus, the zoomed-out part highlights two of them. It is worth noting that aliasing cannot be reliably detected through visual inspection of $\mathrm{V_M^W}$, which highlights the importance of the spectral-based aliasing detection.

The W-band $\mathrm{V_M^{De}}$ obtained with the IntB-DF approach (Fig. 11d) exhibits no sharp transitions at 2000 and 3800 m anymore, as seen in $\mathrm{V_M^W}$. In addition, according to the *Dealiasing flag* in Fig. 11c, almost all profiles were accurately corrected, indicating the robustness of the IntB-DF approach. Only a negligible percentage of 0.0025% of profiles were flagged with at least one "Suspicious" pixel. To be conservative, "Suspicious" pixels and their surroundings may require a double check inspection, since either a range discontinuity (see Sec. 4.1) or unflagged aliasing may ocurr in the DVS. The success frequency (F_s) is defined for each time step as the fraction of range gates for which data from the original $\mathrm{V_M^W}$ or the single-frequency dealiased $\mathrm{V_M^{De}}$ agree with the IntB-DF reference $\mathrm{V_M^{De}}$ within a tolerance of 0.5 m s^{-1}. The resulting F_s values are shown in Fig. 11e. This tolerance is selected because differences in the spectral shifting (defined in Sec. 4.1) between IntB and IterBU methods lead to small differences in $\mathrm{V_M}$, especially in regions of low SNR. Additionally, in order to avoid comparisons in cases when observations of Ka and W band are significantly different, leading to issues in IntB-DF dealiasing (see Sec. 5.1), differences in spectral width between Ka and W-band larger than the 99.9th percentile obtained from the complete hour dataset are filtered out. This high percentile is used since significant difference in multiple spectral peaks between both bands seems to rarely occur. Also, suspicious profiles given by Fig. 11c were filtered out and the Ka-band aliasing mask derived at the *Aliasing detection* step is used to remove cases affected by aliasing and artifacts, as discussed in Sec. 5.1.

A sensitivity analysis was performed to assess the influence of the tolerance threshold on the success rate for the analyzed period between 08:00 and 09:00 UTC, defined as the number of accurately corrected profiles divided by the total number of profiles. The criteria for selecting corrected profiles is defined as F_s larger than 99%, and the success rate was analyzed for different tolerances. A convergence in the IterBU success rate was found for a tolerance around 0.5 m s^{-1}. For this value, Fig. 11e shows that the SF approaches almost perfectly corrected the whole dataset, except for a few profiles for IterBU and IntB-SFT around a region of strong attenuation, between 08:20 and 08:23 UTC. This is expected in regions of strong attenuation, as discussed in the spectrum assessment in Sec. 5.1. However, IntB-SF, IntB-SFT, and IterBU have percentages of success of 99.6%, 99.2%, and 98.6%, respectively, demonstrating the potential of SF approaches. Additionally, range and time continuity constraints do not exhibit a significant improvement in dealiasing. For the IterBU, this can be attributed to the

https://doi.org/10.5194/egusphere-2026-5139
Preprint. Discussion started: 9 September 2026

lack of a quality control step for the first guess. As a result, any inaccuracies present in the initial reference range gate are propagated up to the cloud-top. In contrast, the IntB-SFT includes a quality check that evaluates whether the first guess derived from previous profiles is suitable for use trough the *Dealiasing flag*. Nevertheless, this flag is not guaranteed to identify all residual artifacts in previously dealiased profiles. While this limitation is negligible for this case, it may become more relevant under more challenging conditions. Furthermore, for this particular case, the application of range and time constraints results in slightly decreased performance.

https://doi.org/10.5194/egusphere-2026-5139
Preprint. Discussion started: 9 September 2026

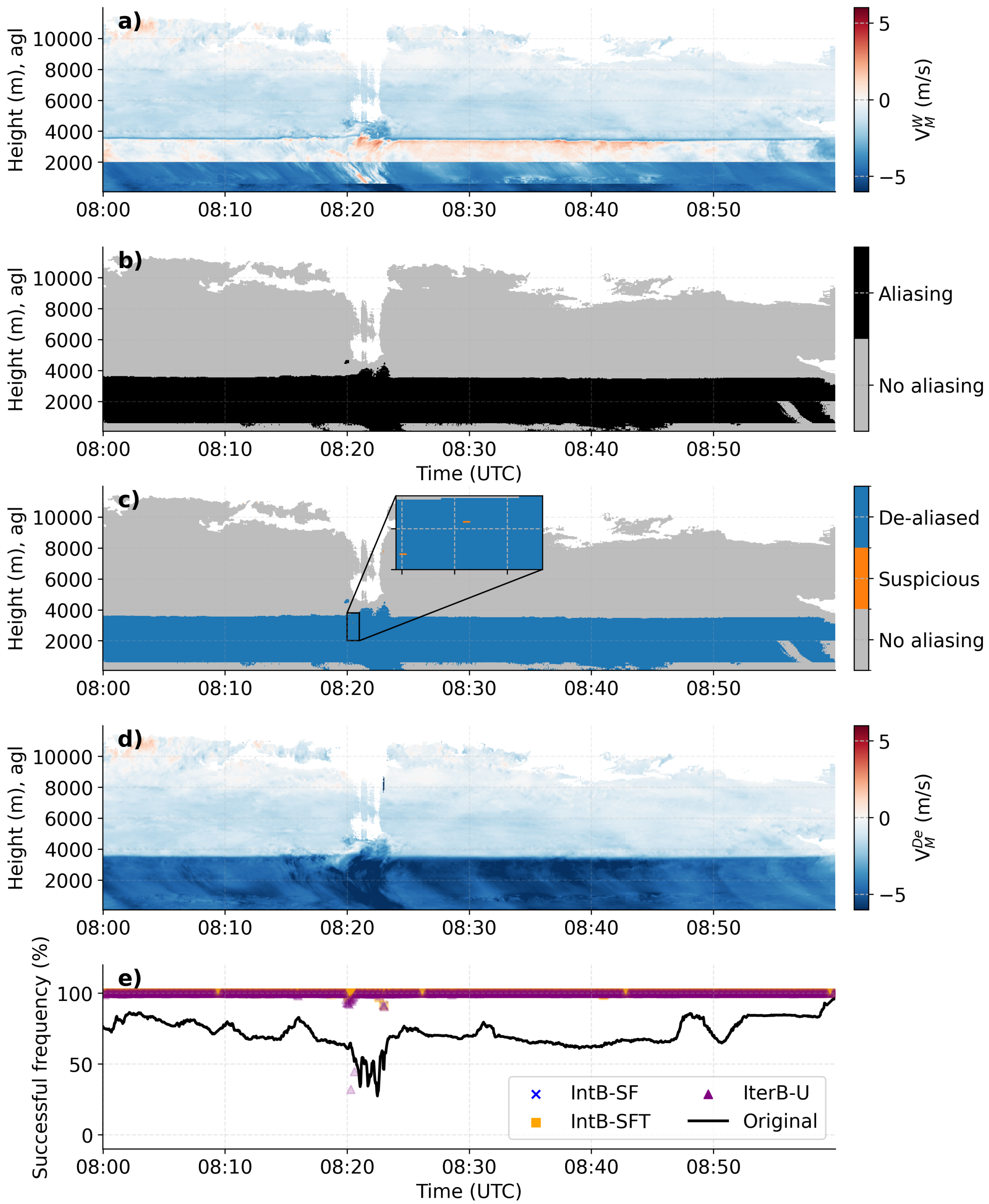

Figure 11. Time series observed by W-JOYDURADO on 01 August 2024 between 08:00 and 09:00 UTC: (a) original mean Doppler velocity V_M; (b) aliasing mask; (c) dealiasing flag; (d) mean Doppler velocity dealiased using IntB-DF; (e) success frequency F_s of the standalone approaches relative to the IntB-DF reference.

https://doi.org/10.5194/egusphere-2026-5139
Preprint. Discussion started: 9 September 2026

To further evaluate the performance of the different dealiasing approaches, a more challenging scenario is analyzed. Fig. 12a shows continuous observations of original V_M^W between 00:00 and 01:00 UTC by W-NEBULA on 29 August 2024. This figure displays a case that exhibits strong attenuation and intense downdrafts and updrafts, which are indicators of challenging aliasing cases as discussed in the previous section. This is observed by sharp discontinuities in the data and the vertical variability of V_M^W. Also, Fig. 12b shows a more heterogeneous aliasing pattern than the W-JOYDURADO case, distributed across several cloud regions. Consequently, a 0.12% of profiles processed with IntB-DF approach contain at least one pixel flagged as "Suspicious" (Fig. 12c). Besides the small percentage, it is much higher than that obtained for the W-JOYDURADO, showing the greater complexity of this cloud. This is consistent with the individual spectrogram assessment in Sec. 5, where due to a sensibility issue, pronounced by strong liquid attenuation, DVS's can be wrongly dealiased. Instead, the IntB-DF corrected most aliased range gates, as can be seen in Fig. 12c, where the majority of the pixels displayed corresponds to a reliable dealiasing, i.e., marked as "Dealiased". Consequently, the resulting V_M^{De} shown in Fig. 12d displays a much smoother structure than the original V_M^W.

Fig. 12e displays the same F_s discussed for W-JOYDURADO (Fig. 11e), also obtained for a tolerance of 0.5 m s^{-1}, and taking into account the differences in S_w between Ka and W-band. Therefore, RADALIA yields a large success percentage for IntB-SF, IntB-SFT, and IterBU, which are 71.9%, 73.4%, and 75%, respectively, being all above 70%. As for the W-JOYDURADO case, the results indicate no significant improvement in the success rate when including time and range continuity constraints. Although IterBU achieves the highest overall success frequency, it also exhibits periods where its performance becomes worse than that of the original data. It is shown in Fig. 12e by IterBU frequency values below the black line between approximately 00:00–00:05, 00:15–00:25, and 00:40–01:00 UTC. Overall, 9.0% of the profiles processed with IterBU perform worse than the original data, compared with only 1.4% and 1.9% for IntB-SF and IntB-SFT, respectively. These failures are attributed to the propagation of errors from a certain range gate where the first guess is inaccurate and subsequently propagated to the cloud top. Consequently, IterBU is the approach most susceptible to severe error propagation when the continuity assumption is violated. Nevertheless, IterBU performed particularly well in general, even in the strong attenuation region between 00:30 and 00:40 UTC, where IntB-SF and IntB-SFT perform the worst. In this interval, these two SF approaches produced worse results than the original data, but they are less impacted than IterBU. This is because the errors in IntB-SF and IntB-SFT are primarily associated with propagation in the time dimension, whereas a verification step (see Sec. 4.1.1) was implemented to minimize the propagation of errors throughout the entire time series.

https://doi.org/10.5194/egusphere-2026-5139
Preprint. Discussion started: 9 September 2026

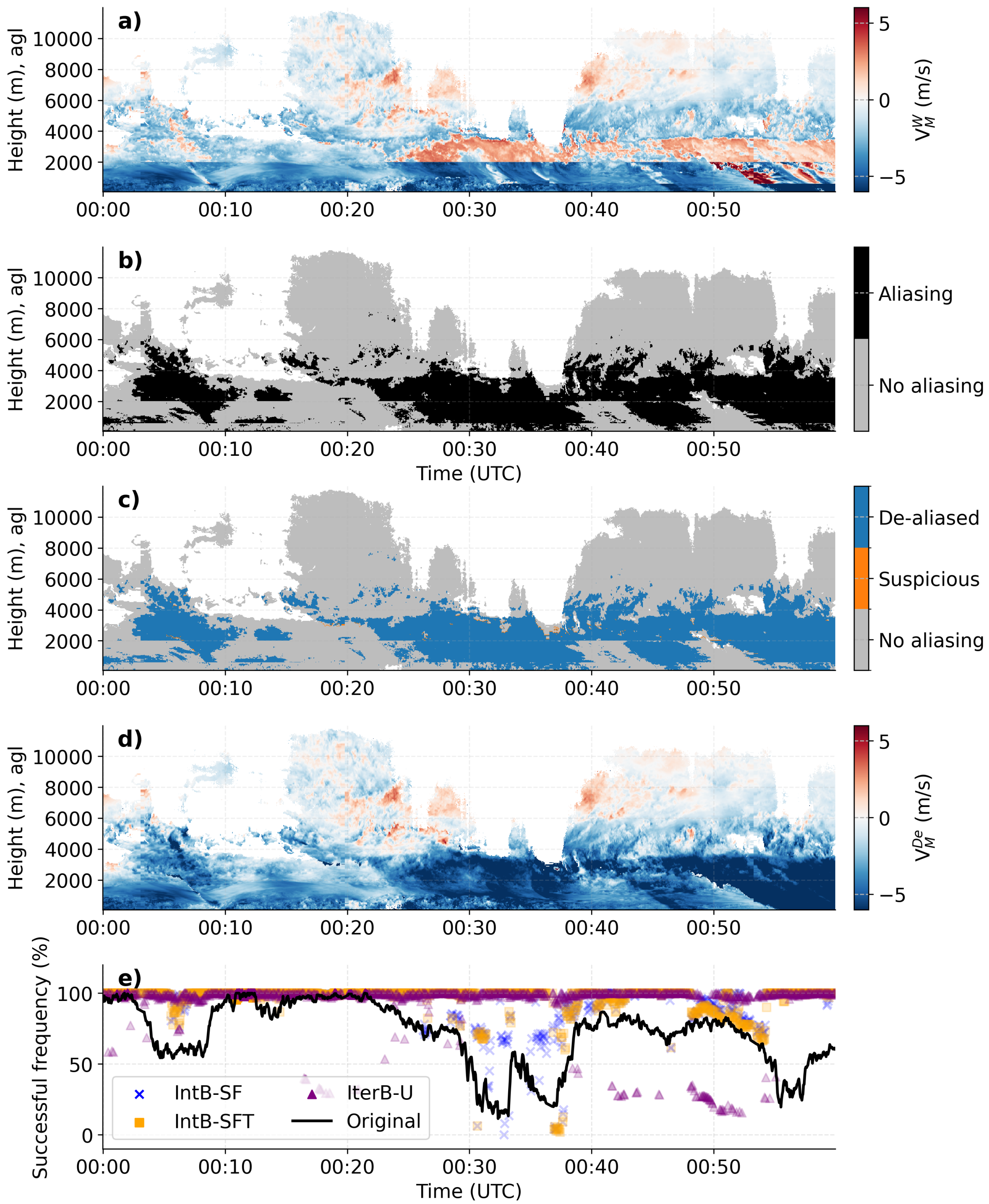

Figure 12. Same as Fig. 11, but for W-NEBULA at the AGORA station on 29 August 2024.

https://doi.org/10.5194/egusphere-2026-5139
Preprint. Discussion started: 9 September 2026

6 Summary and outlook

This study presents RADALIA, a tool for aliasing detection and correction (dealiasing) of Doppler velocity spectra from cloud Doppler radars. This tool significantly enhances the extraction of comprehensive information from DVS moments. The paper presents the operating principles of RADALIA for cloud radar applications and assesses its capabilities and limitations. It currently supports RPG-FMCW radar data and is publicly available, facilitating straightforward access, application, and further development by the wider scientific community.

The assessment of the algorithm is performed in two different locations using DF-DCR observations from identical instruments and radar settings at two ACTRIS-CCRES stations: AGORA and JOYCE. The chosen cloud regimes at both stations are quite different; at JOYCE a relatively straightforward case for DVS dealiasing is observed, with spectrograms generally exhibiting smooth transitions in DVS shape (i.e., changes in hydrometeor population) with height. In contrast, the cloud regime selected at AGORA represents a more challenging dealiasing case, characterized by complex spectrograms with multiple hydrometeor populations, abrupt transitions with height, and strong attenuation.

RADALIA demonstrates consistent performance under simple spectral conditions. Overall, all evaluated methods are suitable for operational applications. The IntB-DF configuration provides the most reliable solution when auxiliary radar observations are available, whereas IntB-SF offers a robust standalone alternative. Particularly, the standalone approaches based on interpolation, temporal continuity, and range continuity (i.e., IntB-SF, IntB-SFT, and IterBU, respectively) achieved near perfect agreement with the IntB-DF reference approach (98.6 % to 99.6 %).

Under more complex spectral conditions, all methods still achieved success rates above 70 %. The obtained success rates in these challenging scenarios, characterized by strong attenuation and the coexistence of multiple hydrometeor populations with distinct fall velocities, still remain quite promising. These findings highlight the importance of accurately dealiasing complex spectra, of which depends on cloud microphysics, dynamics, and detection limitations, and underline the need for careful method selection when extending the analysis to larger and more diverse datasets.

Among the tested approaches, IterBU is particularly promising for implementation in ACTRIS cloud target classification due to its computational efficiency and significantly faster processing, whereas the IntB methods provide a more configurable framework, offering quality-control information and reliability estimates that allow expert users to fine-tune the dealiasing process and adapt it to different observational scenarios. The encouraging results obtained in this study support the ongoing implementation of RADALIA within the Cloudnet processing chain, with the potential to enhance the quality and reliability of cloud radar Doppler products.

Beyond cloud-radar processing itself, RADALIA has the potential to support calibration and validation of satellite-based observations. By correcting aliased Doppler velocity spectra and improving the retrieval of Doppler moments, the algorithm can contribute to more accurate comparisons between ground-based and spaceborne radar observations. Furthermore, correctly dealiased data facilitate the application of spectral peak separation techniques (Vogl et al., 2024), allowing the retrieval of Doppler moments and polarimetric variables associated with distinct hydrometeor populations. This capability opens new

https://doi.org/10.5194/egusphere-2026-5139
Preprint. Discussion started: 9 September 2026

opportunities for investigating cloud microphysical processes and improving the characterization of mixed-phase and precipitating clouds.

In the light of the findings presented in this paper, RADALIA has the potential to enhance higher level cloud-radar products by improving the quality of the DVS, thereby reducing the uncertainties in hydrometeor classification, microphysical retrievals and cloud statistics. Future work should focus on extending its applicability beyond RPG-FMCW systems to other cloud radar systems, including MIRA radars, and on conducting comprehensive validation studies using large and diverse datasets available through Cloudnet. Future developments should also address the adaptation of the methodology to scanning radar observations, thereby broadening its applicability to a wider range of operational and research cloud radar networks.

Code and data availability. The Cloudnet data used in this study are provided by the ACTRIS Cloud Remote Sensing Data Centre Unit (Cloudnet-CLU), Finnish Meteorological Institute (FMI). The data are available under a CC BY 4.0 licence via the ACTRIS Cloudnet portal: https://cloudnet.fmi.fi. DOI: https://doi.org/10.21105/joss.02123, accessed on 10 January 2024. The RADALIA source code used in this study is publicly available through GitHub (https://github.com/matheustolentino/radalia).

Author contributions. MT, LP, JABA, and MJGM conceptualized the study. MT and LP developed the RADALIA tool and IntB algorithm, while TS, ST, and EO developed the IterBU algorithm implemented within RADALIA. MT carried out the formal analysis. MT, LP, JABA, and MJGM contributed to the interpretation of the results and the scientific discussion. MT prepared the original manuscript draft, which was reviewed and edited by all authors. JABA and MJGM supervised the work and acquired funding

Acknowledgements. This work is part of the Spanish national projects PID2022-142708NA-I00 and PID2021-128008OB-I00 funded by MICIU/AEI /10.13039/501100011033/FEDER, UE. It has been partially supported by national infrastructure programs EQC2019-006192-P and EQC2019-006423-P. J. A. Bravo-Aranda acknowledges support from the José Castillejo Mobility Grant for Young Doctors (CAS22/00292), funded by the Spanish Ministry of Universities. We also acknowledge ACTRIS and the ACTRIS Cloud Remote Sensing Data Centre Unit (Cloudnet-CLU) operated by the Finnish Meteorological Institute for providing access to the cloud remote sensing datasets used in this study, available for download from https://cloudnet.fmi.fi (last access: February 2026). Parts of the text in this manuscript were generated and/or edited with the assistance of artificial intelligence tools (e.g., ChatGPT, Scite). The authors reviewed and take full responsibility for the content of the manuscript.

https://doi.org/10.5194/egusphere-2026-5139
Preprint. Discussion started: 9 September 2026

References

Bargen, D. W. and Brown, R. C.: Interactive radar velocity unfolding, in: Preprints, 19th Conference on Radar Meteorology, pp. 278–283, American Meteorological Society, Miami, FL, 1980.

Benjamin M. Courtier, Alessandro Battaglia, and Kamil Mróz: Advantages of G-band radar in multi-frequency liquid-phase microphysical retrievals, Atmospheric Measurement Techniques, https://doi.org/10.5194/amt-17-6875-2024, 2024.

Bergen, W. R. and Albers, S. C.: Two- and Three-Dimensional De-aliasing of Doppler Radar Velocities, Journal of Atmospheric and Oceanic Technology, 1988.

Eilts, M. D. and Smith, S. D.: Efficient Dealiasing of Doppler Velocities Using Local Environment Constraints, Journal of Atmospheric and Oceanic Technology, 1990.

Feuillard, N., Toledo Bittner, F., Pfitzenmaier, L., Ribaud, J.-F., Delanoë, J., Haeffelin, M., and Dupont, J.-C.: Validation of EarthCARE CPR reflectivity using the ACTRIS cloud radar network, EGUsphere, 2026, 1–36, https://doi.org/10.5194/egusphere-2026-925, 2026.

Haase, G. and Landelius, T.: Dealiasing of Doppler Radar Velocities Using a Torus Mapping, Journal of Atmospheric and Oceanic Technology, 2004.

Hennington, L.: Reducing the Effects of Doppler Radar Ambiguities, Journal of Applied Meteorology and Climatology, 1981.

Hildebrand, P. H. and Sekhon, R. S.: Objective Determination of the Noise Level in Doppler Spectra, Journal of Applied Meteorology and Climatology, 13, 808–811, https://doi.org/10.1175/1520-0450(1974)013<0808:ODOTNL>2.0.CO;2, 1974.

Illingworth, A. J., Hogan, R. J., O'Connor, E. J., Bouniol, D., Brooks, M. E., Delanoé, J., Donovan, D. P., Eastment, J. D., Gaussiat, N., Goddard, J. W. F., Haeffelin, M., Baltink, H. K., Krasnov, O. A., Pelon, J., Piriou, J.-M., Protat, A., Russchenberg, H. W. J., Seifert, A., Tompkins, A. M., van Zadelhoff, G.-J., Vinit, F., Willén, U., Wilson, D. R., and Wrench, C. L.: Cloudnet, Bulletin of the American Meteorological Society, https://doi.org/10.1175/BAMS-88-6-883, 2007.

James, C. N. and Houze, R. A.: A Real-Time Four-Dimensional Doppler Dealiasing Scheme, Journal of Atmospheric and Oceanic Technology, 2001.

Jing, Z. and Wiener, G.: Two-Dimensional Dealiasing of Doppler Velocities, Journal of Atmospheric and Oceanic Technology, 1993.

Joe, P. and May, P. T.: Correction of Dual PRF Velocity Errors for Operational Doppler Weather Radars, Journal of Atmospheric and Oceanic Technology, 2003.

Kneifel, S., Kollias, P., Battaglia, A., Leinonen, J., Maahn, M., Kalesse, H., and Tridon, F.: First observations of triple-frequency radar Doppler spectra in snowfall: Interpretation and applications, Geophysical Research Letters, 43, 2225–2233, https://doi.org/10.1002/2015GL067618, 2016.

Kollias, P., Bharadwaj, N., Clothiaux, E. E., Lamer, K., Oue, M., Hardin, J., Isom, B., Lindenmaier, I., Matthews, A., Luke, E. P., Giangrande, S. E., Johnson, K., Collis, S., Comstock, J., and Mather, J. H.: The ARM Radar Network: At the Leading Edge of Cloud and Precipitation Observations, Bulletin of the American Meteorological Society, https://doi.org/10.1175/BAMS-D-18-0288.1, 2020.

Krasnov, O. A., Zhang, Q., and Yarovoy, A.: Polarimetric Calibration of an FMCW Doppler Radar with Dual-Orthogonal Signals, in: 2023 IEEE Conference on Antenna Measurements and Applications (CAMA), pp. 312–317, https://doi.org/10.1109/CAMA57522.2023.10352897, 2023.

Küchler, N., Kneifel, S., Löhnert, U., Kollias, P., Czekala, H., and Rose, T.: A W-Band Radar–Radiometer System for Accurate and Continuous Monitoring of Clouds and Precipitation, Journal of Atmospheric and Oceanic Technology, https://doi.org/10.1175/JTECH-D-17-0019.1, 2017.

Laj, P., Myhre, C. L., Riffault, V., Amiridis, V., Fuchs, H., Eleftheriadis, K., Petäjä, T., Salameh, T., Kivekäs, N., Juurola, E., Saponaro, G., Philippin, S., Cornacchia, C., Arboledas, L. A., Baars, H., Claude, A., Mazière, M. D., Dils, B., Dufresne, M., Evangeliou, N., Favez, O., Fiebig, M., Haeffelin, M., Herrmann, H., Höhler, K., Illmann, N., Kreuter, A., Ludewig, E., Marinou, E., Möhler, O., Mona, L., Murberg, L. E., Nicolae, D., Novelli, A., O'Connor, E., Ohneiser, K., Altieri, R. M. P., Picquet-Varrault, B., Pinxteren, D. v., Pospichal, B., Putaud, J.-P., Reimann, S., Siomos, N., Stachlewska, I., Tillmann, R., Voudouri, K. A., Wandinger, U., Wiedensohler, A., Apituley, A., Comerón, A., Gysel-Beer, M., Mihalopoulos, N., Nikolova, N., Pietruczuk, A., Sauvage, S., Sciare, J., Skov, H., Svendby, T., Swietlicki, E., Tonev, D., Vaughan, G., Zdimal, V., Baltensperger, U., Doussin, J.-F., Kulmala, M., Pappalardo, G., Sundet, S. S., and Vana, M.: Aerosol, Clouds and Trace Gases Research Infrastructure – ACTRIS, the European research infrastructure supporting atmospheric science, Bulletin of the American Meteorological Society, https://doi.org/10.1175/BAMS-D-23-0064.1, place: Boston MA, USA Publisher: American Meteorological Society, 2024.

Löhnert, U., Schween, J. H., Acquistapace, C., Ebell, K., Maahn, M., Barrera-Verdejo, M., Hirsikko, A., Bohn, B., Knaps, A., O'Connor, E., Simmer, C., Wahner, A., and Crewell, S.: JOYCE: Jülich Observatory for Cloud Evolution, Bulletin of the American Meteorological Society, 96, 1157–1174, https://doi.org/10.1175/BAMS-D-14-00105.1, 2015.

Luke, E. P. and Kollias, P.: Separating Cloud and Drizzle Radar Moments during Precipitation Onset Using Doppler Spectra, Journal of Atmospheric and Oceanic Technology, https://doi.org/10.1175/JTECH-D-11-00195.1, 2013.

Luke, E. P., Yang, F., Kollias, P., Vogelmann, A. M., and Maahn, M.: New insights into ice multiplication using remote-sensing observations of slightly supercooled mixed-phase clouds in the Arctic, Proceedings of the National Academy of Sciences, 118, e2021387 118, https://doi.org/10.1073/pnas.2021387118, 2021.

Maahn, M. and Kollias, P.: Improved Micro Rain Radar snow measurements using Doppler spectra post-processing, Atmospheric Measurement Techniques, 5, 2661–2673, https://doi.org/10.5194/amt-5-2661-2012, 2012.

Merritt, M. W.: Automatic velocity dealiasing for real-time applications, in: Proceedings of the 22nd Conference on Radar Meteorology, pp. 528–533, American Meteorological Society, Zurich, Switzerland, 1984.

Myagkov, A., Seifert, P., Bauer-Pfundstein, M., and Wandinger, U.: Cloud radar with hybrid mode towards estimation of shape and orientation of ice crystals, Atmospheric Measurement Techniques, 9, 469–489, https://doi.org/10.5194/amt-9-469-2016, 2016.

Ortiz-Amezcua, P., Martínez-Herrera, A., Manninen, A. J., Pentikäinen, P. P., O'Connor, E. J., Guerrero-Rascado, J. L., and Alados-Arboledas, L.: Wind and Turbulence Statistics in the Urban Boundary Layer over a Mountain–Valley System in Granada, Spain, Remote Sensing, 14, 2321, https://doi.org/10.3390/rs14102321, 2022.

Oue, M., Kollias, P., Ryzhkov, A., and Luke, E. P.: Toward Exploring the Synergy Between Cloud Radar Polarimetry and Doppler Spectral Analysis in Deep Cold Precipitating Systems in the Arctic, Journal of Geophysical Research: Atmospheres, 123, 2797–2815, https://doi.org/10.1002/2017JD027717, 2018.

Pfitzenmaier, L., Unal, C. M. H., Dufournet, Y., and Russchenberg, H. W. J.: Observing ice particle growth along fall streaks in mixed-phase clouds using spectral polarimetric radar data, Atmospheric Chemistry and Physics, 18, 7843–7862, https://doi.org/10.5194/acp-18-7843-2018, 2018.

Pfitzenmaier, L., Kollias, P., Risse, N., Schirmacher, I., Puigdomenech Treserras, B., and Lamer, K.: Orbital-Radar v1.0.0: a tool to transform suborbital radar observations to synthetic EarthCARE cloud radar data, Geoscientific Model Development, 18, 101–115, https://doi.org/10.5194/gmd-18-101-2025, 2025.

Ray, P. S. and Ziegler, C.: De-Aliasing First-Moment Doppler Estimates, Journal of Applied Meteorology and Climatology, 1977.

https://doi.org/10.5194/egusphere-2026-5139
Preprint. Discussion started: 9 September 2026

Tetoni, E., Ewald, F., Hagen, M., Köcher, G., Zinner, T., and Groß, S.: Retrievals of ice microphysical properties using dual-wavelength polarimetric radar observations during stratiform precipitation events, Atmospheric Measurement Techniques, 15, 3969–3999, https://doi.org/10.5194/amt-15-3969-2022, 2022.

Tolentino, M., Bravo-Aranda, J. A., Guerrero-Rascado, J. L., Navas-Guzmán, F., Pérez-Ramírez, D., Alados-Arboledas, L., and Granados-Muñoz, M. J.: Long-term cloud characterization at the AGORA ACTRIS-CCRES station using a novel classification algorithm, EGUsphere, pp. 1–37, https://doi.org/10.5194/egusphere-2025-5239, 2025.

Tukiainen, S., O'Connor, E., and Korpinen, A.: CloudnetPy: A Python package for processing cloud remote sensing data, Journal of Open Source Software, 5, 2123, https://doi.org/10.21105/joss.02123, 2020.

Unal, C. M. H. and Moisseev, D. N.: Combined Doppler and Polarimetric Radar Measurements: Correction for Spectrum Aliasing and Nonsimultaneous Polarimetric Measurements, Journal of Atmospheric and Oceanic Technology, 2004.

Vogl, T., Radenz, M., Ramelli, F., Gierens, R., and Kalesse-Los, H.: PEAKO and peakTree: Tools for detecting and interpreting peaks in cloud radar Doppler spectra – capabilities and limitations, https://doi.org/10.5194/egusphere-2024-837, 2024.

von Terzi, L., Dias Neto, J., Ori, D., Myagkov, A., and Kneifel, S.: Ice microphysical processes in the dendritic growth layer: a statistical analysis combining multi-frequency and polarimetric Doppler cloud radar observations, Atmospheric Chemistry and Physics, 22, 11 795–11 821, https://doi.org/10.5194/acp-22-11795-2022, 2022.